

The Nearby Evolved Stars Survey: I. JCMT/SCUBA-2 Sub-millimetre detection of the detached shell of U Antliae^{*}

Thavisha E. Dharmawardena^{1,2†}, Sundar Srinivasan¹, F. Kemper¹, Peter Scicluna¹, Jonathan P. Marshall¹, Jan G. A. Wouterloot³, Jane Greaves⁴, Steven R. Goldman⁵, Hideyuki Izumiura⁶, Jacco Th. van Loon⁷, Mikako Matsuura⁴, Iain McDonald⁸, Sofia H. J. Wallström¹, Albert Zijlstra^{8,9}, Jan Cami^{10,11}, Jinhua He¹², Wayne Holland¹³, Olivia Jones¹³, Hyosun Kim¹⁴, Hiroko Shinnaga¹⁵, Alfonso Trejo¹

¹ Academia Sinica Institute of Astronomy and Astrophysics, 11F of AS/NTU Astronomy-Mathematics Building, No.1, Sec. 4, Roosevelt Rd, Taipei 10617, Taiwan, R.O.C.

² Graduate Institute of Astronomy, National Central University, 300 Zhongda Road, Zhongli 32001, Taoyuan, Taiwan, R.O.C.

³ East Asian Observatory, 660 N A'ohoku Place, Hilo, Hawaii 96720, USA.

⁴ School of Physics and Astronomy, Cardiff University, 4 The Parade, Cardiff CF24 3AA, UK.

⁵ STScI, 3700 San Martin Drive, Baltimore, MD 21218 USA

⁶ NAOJ - To be completed!!!

⁷ Lennard-Jones Laboratories, Keele University, ST5 5BG, UK.

⁸ Jodrell Bank Centre for Astrophysics, Alan Turing Building, University of Manchester, Manchester, M13 9PL, UK.

⁹ Laboratory for Space Research, University of Hong Kong, Pokfulam Road, Hong Kong

¹⁰ Department of Physics and Astronomy and Centre for Planetary Science and Exploration (CPSX), The University of Western Ontario, London, ON N6A 3K7, Canada

¹¹ SETI Institute, 189 Bernardo Ave, Suite 100, Mountain View, CA 94043, USA

¹² YNAO - To be completed!!!

¹³ UK Astronomy Technology Centre, Royal Observatory, Blackford Hill, Edinburgh EH9 3HJ, UK

¹⁴ KASI - To be completed!!!

¹⁵ Kagoshima - To be completed!!!

11 September 2018

ABSTRACT

Key words: stars: AGB and post-AGB – stars: circumstellar matter – stars: mass-loss – stars: individual: U Ant

1 INTRODUCTION

In the final stages of their evolution stars expel their outer layers enriched with the products of nucleosynthesis into the interstellar medium (ISM). For intermediate-mass stars ($1M_{\odot} \leq M \leq 8M_{\odot}$), the majority of this mass loss occurs while on the Asymptotic Giant Branch (AGB). Collectively, these stars make a considerable contribution to the ISM (Boyer et al. 2012; Karakas & Lattanzio 2014), driving the Milky Way’s chemical evolution and replen-

ishing its dust reservoir. Metals condense and form dust grains in the cool, denser regions of these extended AGB envelopes. Together with gaseous material, this dust is carried by the pulsation-enhanced, radiation-pressure driven winds into the ISM (Höfner & Olofsson 2018).

AGB stars are often treated as quasi-stable systems, without incorporating treatment of their evolution; while their winds are treated as spatially and temporally homogeneous outflows. The existence of complex structures such as elongations, detached shells and bipolar outflows (Zijlstra et al. 2001; Olofsson et al. 2010; Ramstedt et al. 2011; Cox et al. 2012; Maercker et al. 2012), indicates that the true mass loss mechanisms are far more complex than what is currently modelled. Particularly uncertain is the extent to which the stellar wind is enhanced in mass and/or momentum when the star undergoes a thermal pulse (He-shell

* The scripts and reduced data required to reproduce the analysis, figures and tables presented in this paper can be downloaded from https://github.com/Thavisha/UAnt_DetachedShell. The raw data will be made available with the first NESS data release.

† tdharmawardena@asiaa.sinica.edu.tw

flash). Thus, further observational constraints are required before we can statistically model mass loss from AGB stars accurately.

By studying the extended dust emission and comparing it to constant-outflow models and detailed numerical simulations (e.g. [Bowen & Willson 1991](#); [Höfner 2008](#), [Toalá et al.](#), in prep), we can study the properties of this non-uniformity and accurately determine time-variant mass-loss and dust-production rates.

Of the variety of structures shown by AGB stellar envelopes, detached dust shells are among the most striking features. They are thought to result from a period of strong mass loss due to a thermal pulse, during which the star may expand and brighten dramatically for a few centuries ([Willems & de Jong 1988](#); [Vassiliadis & Wood 1994](#); [Marigo et al. 2017](#)). The enhancement in mass-loss rate during the pulse is modelled to be more than an order of magnitude. A faster wind speed during this strong mass loss period means that the older, slower wind in front of the density-enhanced wind is piled up at the shock interface into a shell [Schöier et al. \(2005\)](#). Such a source would be observed as a nearly symmetrical ring of gas and dust surrounding a near hollow region around the star. Similar morphologies have been observed in a number of objects (e.g. [Olofsson et al. 1988, 1990](#); [Izumiura et al. 1996, 1997, 2011](#)).

U Antliae (U Ant) is a C-rich AGB star located at a distance of 268 ± 39 pc ([van Leeuwen 2007](#)). It is surrounded by a well-defined detached shell, estimated to have been expelled by the star 2800 years ago ([Kerschbaum et al. 2010](#)). Independent scattered light, ^{12}CO low-J rotational line emission, and mid-IR and far-IR observations of the detached shell all show a radically different structure. Optical scattered light observations by [González Delgado et al. \(2001, 2003\)](#) show the detached shell separated into four sub-shells at $\sim 25''$, $37''$, $43''$ and $46''$ from the star (hereafter ss1, ss2, ss3, ss4), with the innermost two shells only tentative detections. They derive shell widths of $\sim 3''$, $\sim 6''$, $\sim 3''$ and $\sim 10''$ for ss1, ss2, ss3 and ss4 respectively. These authors find ss3 to be dominated by line-scattered light instead of dust-scattered light indicating that ss3 is dominated by gas instead of dust.

Similarly, [Maercker et al. \(2010\)](#) also observed ss3 and ss4 in optical scattered light at $\sim 43''$ and $\sim 50''$ with shell widths of $\sim 2''$ and $\sim 7''$. They also find ss3 appears faint in dust-scattered light and bright in line-scattered light reaching the same conclusion that ss3 is most-likely dominated by gas. The authors also observe peaks at the positions of ss1 and ss2 in their azimuthally averaged radial profiles. While these peaks could be indeed due the ss1 and ss2, the authors argue that they are more likely due to sub-structure of ss3 and ss4 projected towards the inner regions of the detached shell.

Mid-IR and far-IR observations from AKARI show that the detached shell is dominated by ss3 and ss4 observed in scattered light ([Arimatsu et al. 2011](#)), evidenced by two concentric shells with radii of $44''$ and $50''$. The large beam size of AKARI (FWHMs of $37''$ at $65 \mu\text{m}$ to $61''$ at $160 \mu\text{m}$) most likely smears out the emission from ss4 extending it to the observed $50''$ size when comparing the scattered light ss3 and ss4. Similarly far-IR observations from Herschel/PACS appear to be dominated by ss3 ([Cox et al. 2012](#)).

The azimuthally averaged radial profile of the APEX

$^{12}\text{CO}(3-2)$ observations derived by [Maercker et al. \(2010\)](#) clearly peaks at the location of ss3 and has a measured shell width of $\sim 2.6''$. High spatial resolution ($1.5''$ resolution) ALMA $^{12}\text{CO}(2-1)$ and $(1-0)$ observations by [Kerschbaum et al. \(2017\)](#) also only detect a single CO gas shell coinciding well with ss3. The CO shell is located at $42.5''$ from the central source and has a measured width of $\sim 5''$. It is also observed to have visible filamentary substructure.

Based on these observations at multiple wavelengths in both gas and dust it is suggested that ss1, ss2 and ss4 are gas poor hence only visible in the dust continuum. Sub-shell 3 deviates from the other three sub-shells and is suggested to be gas dominated ([Maercker et al. 2010](#); [Kerschbaum et al. 2017](#)). A schematic diagram and accompanying table of the published sub-shell radii are presented in Fig. A1 and Tab. A1 in the appendix.

As mentioned above, [Maercker et al. \(2010\)](#) suggest that ss3 and ss4 are real, while ss1 and ss2 are filamentary sub-structures of ss3 and ss4 projected against the inner regions of the detached shell. The small distance between ss3 and ss4 and the corresponding time scales (~ 110 yr [Maercker et al. 2010](#)) suggest that these sub-shells could not have occurred due to multiple thermal pulses. The most likely scenario is a single thermal pulse ~ 2800 yrs ago gave rise to the detached shell following which a secondary mechanism shaped the single detached shell into the multiple sub-shells observed ([Maercker et al. 2010](#)).

A model for multiple shell formation in AGB and post-AGB stars was proposed by [Simis et al. \(2001\)](#). They suggest alternating dust and gas shells 200 – 400 years apart formed as a result of dust and gas decoupling. In a similar vein for U Ant, [Maercker et al. \(2010\)](#) proposed the splitting of a single detached shell (located at the position of ss3) into two is an effect of gas-grain decoupling due to varying expansion velocities, resulting in a single, gas-rich sub-shell and a dust component at larger radii due to the higher expansion velocity. In this scenario the gas velocity slows down in the wind collision region while the dust sails through.

However if ss1 and ss2 are real, an as-of-yet unknown mechanism is required to explain their formation. One possibility is that instabilities at the interaction between the fast and slow winds may have created multiple shock fronts with dust decoupling in the swept back shock, resulting in ss1 and ss2 ([González Delgado et al. 2001](#); [Schöier et al. 2005](#); [Kerschbaum et al. 2017](#)). The presence of filamentary structure in the gas-rich shell in the ALMA observation provides evidence for a reverse shock to have occurred. Another is that these shells could be a result of density and velocity modulations which took place during the thermal pulse [Villaver et al. \(2002\)](#); [Maercker et al. \(2010\)](#).

While U Ant is well studied from the optical to the far-IR, only a few sub-mm continuum observations of the source exists. Archival observations obtained using the JCMT/SCUBA instrument (the predecessor to SCUBA-2) in 1997 (PI: Greaves) were never published, and do not clearly show the detached shell due to a low signal-to-noise ratio. U Ant was also part of a sample of three detached shell sources studied by [Maercker et al. \(2018\)](#) at $870 \mu\text{m}$ using APEX/LABOCA.

In their studies [Maercker et al. \(2018\)](#) report a sub-mm excess in the detached shell when comparing the observed fluxes to the output from radiative transfer models derived

by combining data from the optical to the far-IR and extrapolating to the sub-mm. They measure an excess which is 2.3 ± 0.3 times greater than the model predictions. However, while they present several hypotheses they are unable to conclusively identify the origin of the excess, which may be alleviated by higher angular resolution observations.

In this paper we present new resolved submillimetre dust continuum detections of the detached shell of U Ant, obtained with the James Clerk Maxwell Telescope's (JCMT) Sub-millimetre Common-User Bolometer Array 2 (SCUBA-2; Holland et al. (2013)) instrument, as part of the Nearby Evolved Stars Survey (NESS; Scicluna et al., *in prep.*). Using this data we study the dust properties and masses in this unique detached shell source. This allows us to approximate the dust mass loss and age of the thermal pulse which gave rise to the detached shell. Using radiative transfer (RT) modelling we will evaluate whether our observations are consistent with the dust distribution over the four sub-shells reported in the optical light observations. Lastly we inspect the observations and results for the possible presence of the sub-mm excess previously reported.

As part of the NESS data release, the raw SCUBA-2 data used in the paper will be available in the near future, while the scripts and reduced data required to reproduce the analysis, figures and tables presented in this paper can be downloaded from https://github.com/Thavisha/UAnt_DetachedShell.

2 OBSERVATIONS AND DATA REDUCTION

U Ant was observed on 18/01/2018 as part of the NESS project (program ID: M17BL002) with the SCUBA-2 receiver on the JCMT. The observations were carried out at $450 \mu\text{m}$ (beam FWHM = $7.9''$) and $850 \mu\text{m}$ (beam FWHM = $13''$) using the CV-daisy scan pattern.

We downloaded the raw U Ant SCUBA-2 data from the Canadian Astronomy Data Centre (CADC)¹ data archive where they were stored after observation, and reduced them using the standard JCMT data reduction pipelines available via Starlink² (Currie et al. 2014). Following Dharmawardena et al. (2018), we used the standard *REDUCE_SCAN_ISOLATED_SOURCE* pipeline with a increased mask size of $90''$ instead of the standard $60''$ mask in the pipeline. The mask size was increased in order to ensure artefacts such as negative bowling do not affect the reduced data products.

The resulting $450 \mu\text{m}$ map has an RMS of $0.24 \text{ mJy arcsec}^{-2}$ and a pixel size of $2''$. The $850 \mu\text{m}$ map has an RMS of $0.014 \text{ mJy arcsec}^{-2}$ and a pixel size of $4''$.

We also used Herschel/PACS $70 \mu\text{m}$ and $160 \mu\text{m}$ imaging observations of U Ant, which were taken as part of the Mass-loss of Evolved StarS (MESS) program (Groenewegen et al. 2011). The Herschel data are publicly available for download via the Herschel Science Archive³. Here, we used the Level 2.5 reduced products, the highest available pipeline-reduced data products calibrated using PACS calibration version *PACS_CAL_77.0*.

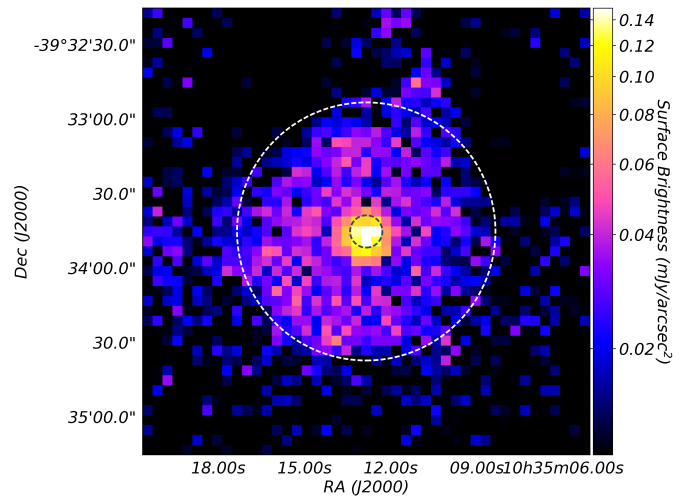


Figure 1. $850 \mu\text{m}$ observation of U Ant. The grey dashed innermost circle represents the FWHM of the SCUBA-2 PSF. The outer dashed white circle represents the 3σ surface brightness extent.

In addition to SCUBA-2 observations there are also 2.1 hr of $850 \mu\text{m}$ SCUBA observations of U Ant obtained in 1997. However as it was noise dominated we could not include it in our study. We present these observations in the appendix.

3 ANALYSIS AND RESULTS

3.1 Surface Brightness Profiles

The $850 \mu\text{m}$ image clearly shows emission extending over the region of the detached shell of U Ant (see Fig. 1).

The surface brightness profiles and residual profiles of U Ant derived using the methods described in Dharmawardena et al. (2018) are shown in Figure 2. The $850 \mu\text{m}$ residual profile of U Ant is dominated by a broad peak in the inner region between $\sim 20''$ and $\sim 40''$. The locations of ss1 and ss2 in scattered light fall within this broad peak. However, we do not observe two distinct sub-shells in this region as those observed in optical scattered light. The profile has a surface brightness extent of $52''$ at 3σ detection limit, including the outermost shell observed in scattered light.

The $450 \mu\text{m}$ residual profile appears to have a peak at $\sim 40''$. The low signal-to-noise of the observation limits our ability to constrain the peak any further.

Analysis of the PACS residual profiles produce clear peaks in the outer region at $\sim 41''$ and $\sim 39''$ for $70 \mu\text{m}$ and $160 \mu\text{m}$ respectively. These two peaks most-likely coincide with ss3 in optical scattered light and the gas-rich shell observed by Kerschbaum et al. (2017). We also see emission at 3σ brightness levels outwards up to the approximate location of ss4.

The total fluxes (central point source + extended component; F_{total}) for U Ant at $450 \mu\text{m}$ and $850 \mu\text{m}$ were measured to be $80 \pm 10 \text{ mJy}$ and $248 \pm 21 \text{ mJy}$ respectively. The flux at $850 \mu\text{m}$ is consistent with a recent $870 \mu\text{m}$ detection with APEX/LABOCA (Maercker et al., 2018, *accepted*, A&A). We compute a flux of $208 \pm 21 \text{ mJy}$ for the extended

¹ <http://www.cadc-ccda.hia-ihaw.nrc-cnrc.gc.ca/en/jcmt/>

² version 2017A

³ <http://www.cosmos.esa.int/web/herschel/science-archive>

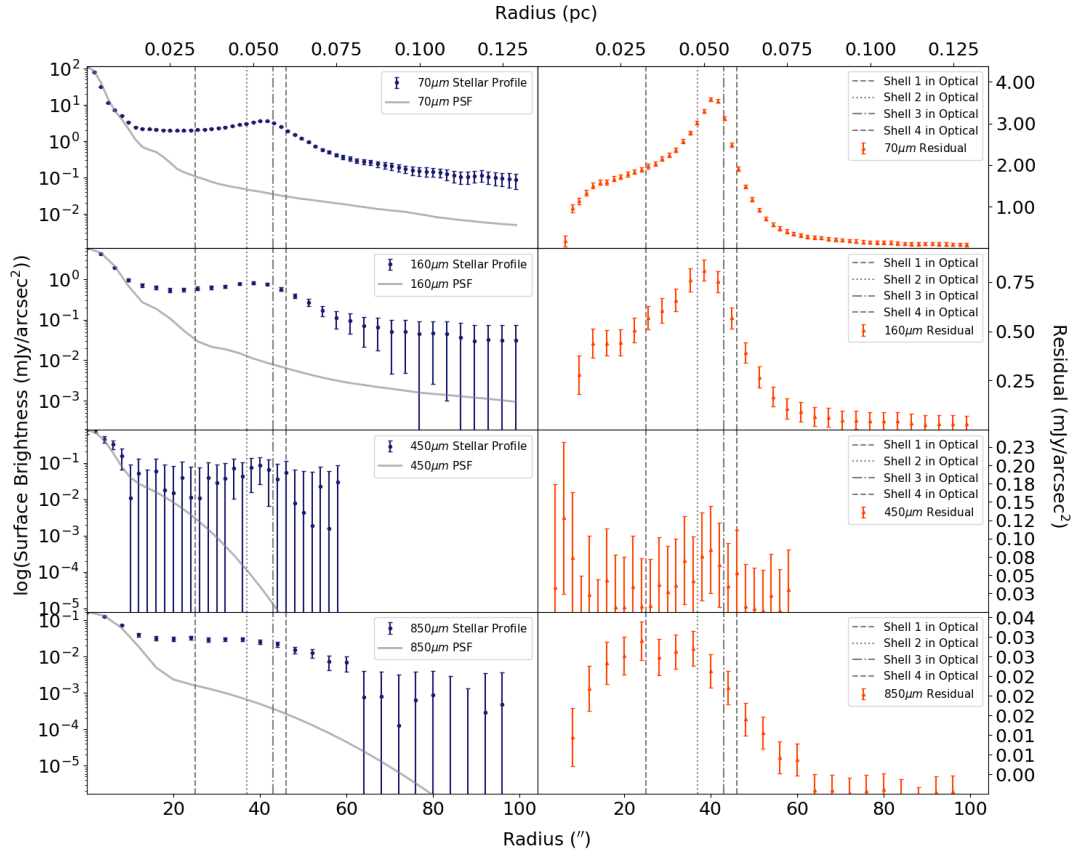


Figure 2. Surface brightness and Residual profiles of U Ant. Right hand panels: The blue dashed lines represent the source surface brightness profiles and the grey solid lines represent the PSF profile of the instrument at the given wavelength; Left hand panels: The orange lines represents the PSF subtracted residual profiles for each wavelength. The four vertical grey lines in this panel represent the four shells observed in the optical.

component of the detached shell at $850\ \mu\text{m}$ by subtracting the central point source flux from the total flux.

3.2 Radial point-to-point Spectral Energy Distribution Fitting

We derive Spectral Energy Distributions (SEDs) at each radial point following the method described by [Dharmawardena et al. \(2018\)](#). We fit the SED in each radial point of the detached shell component with a single-temperature blackbody model modified by an effective emissivity law (e.g., [Hildebrand 1983](#); [Gordon et al. 2014](#)).

In order to carry out the SED fitting we employ the PYTHON package EMCEE, ([Foreman-Mackey et al. 2013](#)), which uses affine-invariant Markov Chain Monte Carlo (MCMC) algorithms to carry out Bayesian inference on the SEDs and the specified model, and find the most probable value for each parameter at every radial point.

We made modifications to the SED fitting MCMC code presented by [Dharmawardena et al. \(2018\)](#). In particular, the limits in the T prior are set to $20\ \text{K} < T < 300\ \text{K}$, with the inner temperature set to $1800\ \text{K}$. We find these modification allow for better converged results for U Ant.

Fitting the model to each point of the radial profiles results in profiles for the dust temperature (T), emissivity spectral index (β), and dust mass column density (Σ). The

resulting T , β and Σ profiles are presented in Figure 3. Due to PSF subtraction at the central position when deriving the residual profile, the innermost $\sim 8''$ of the T , β and Σ profiles are unreliable. We do not include this region in our analysis. By integrating over the Σ profile from $12''$ to $52''$ we derive a total dust mass of $2.2 \times 10^{-4}\ M_{\odot}$ in the extended shell.

As described in Sec. 4.2 of [Dharmawardena et al. \(2018\)](#), the curvature of the fitted modified blackbody is dependent on both β and T . The temperature is constrained by the peak of the SED at each individual radial point, thus by the Wien end of the SED ([Shetty et al. 2009](#)). Hence the T profile is constrained by the shorter far-IR PACS detections. The β profile is constrained by the longer wavelength ($\lambda \geq 300\ \mu\text{m}$) SCUBA-2 detections as it is constrained by the Rayleigh-Jeans tail of the SED ([Doty & Leung 1994](#); [Shetty et al. 2009](#); [Sadavoy et al. 2013](#)). The Σ profile is constrained by either the PACS or the SCUBA-2 detections. Therefore due to non-detections in PACS $160\ \mu\text{m}$ and both SCUBA-2 wavelength observations beyond $\sim 55''$ all three parameter profiles are prior dominated from thereon.

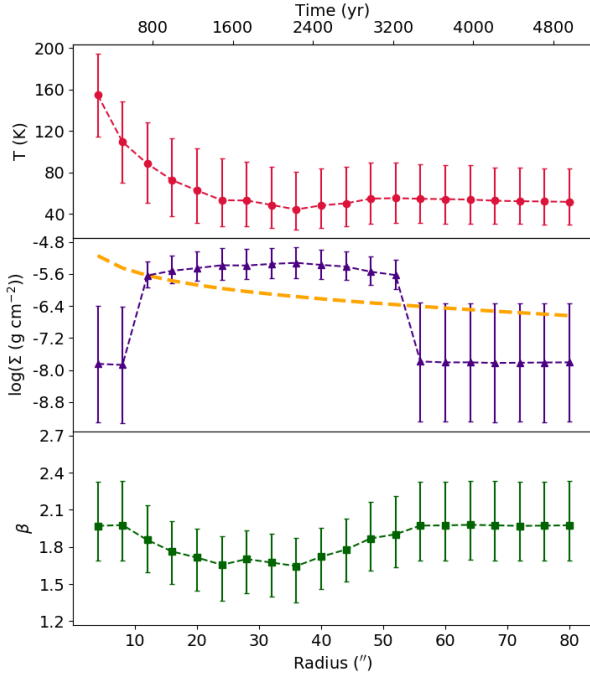


Figure 3. SED fitting results of U Ant; Top: Temperature (T) radial profile of U Ant; Middle: Dust mass column density (Σ) radial profile. Orange dashed line represents the expected dust mass column density for a uniform mass-loss rate; Bottom: The spectral index of dust emissivity (β) profile of U Ant.

3.3 Self-consistent dust radiative transfer modelling

3.4 The attached shell

NEEDS to be rewritten with Sundar’s new models!!

In order to constrain the stellar parameters, we fit the IRAS (Neugebauer et al. 1984; Beichman et al. 1988), AKARI IRC/FIS (Ishihara et al. 2010; Doi et al. 2015), WISE (Wright et al. 2010), and 2MASS (Skrutskie et al. 2006) photometry for U Ant with the Grid of RSG and AGB ModelS (GRAMS; Sargent et al. 2011; Srinivasan et al. 2011). The best-fit models result in a luminosity of $L = (5900 \pm 1000) L_{\odot}$ and an effective temperature of $T_{\text{eff}} = (2800 \pm 100)$ K. The surface gravity of the best-fit models is found to be $\log(g [\text{cm s}^{-2}]) = -0.3$. The mid-IR dust emission is well-reproduced by models with optical depths ranging from 0.001 to 0.004 at $11.3 \mu\text{m}$ (replace with values in the V-band to compare with Kerschbaum2010) and inner shell radii ranging from 3 to 6 times the stellar radius. These results are consistent with those of Kerschbaum et al. (2010). Moreover, the temperature at the inner radius is found to be (1110 ± 180) K, consistent with the 1000 K inner radius temperature assumed by Kerschbaum et al. (2010).

3.5 The detached shell

Before we perform detailed analysis by constructing a large number of detached-shell models, we determine whether we can distinguish between models with various inner and outer radii in the resulting intensity profiles.

As we only see one shell in the submm observations, we assume that the dust is continuously distributed in a shell encompassing the four subshells. Once we obtain higher-resolution observations, we will refine our models to include this information.

Models:

- 1) A “thick” detached shell with the inner and outer radii being fixed, to match the submm observations.
 - 2) All the dust squished into the innermost subshell
 - 3) All the dust squished into the outermost subshell
- If we can exclude model (3), then we can show that there must be dust inward of the canonical subshell everyone else uses. That would be consistent with what we see in the radial profile.

We assume that the circumstellar dust in U Ant is distributed in a spherically-symmetric shell made up of two components: a shell extending from R_{min} to R_{max} and, embedded within this, the detached shell between R_{in} and R_{out} such that $R_{\text{min}} < R_{\text{in}} < R_{\text{out}} < R_{\text{max}}$. We assume that both shells have an inverse-square density profile (corresponding to a constant dust-production rate), but that the density increases by a factor α at R_{in} . In other words,

$$\rho(r) = \begin{cases} \rho(R_{\text{min}}) \left(\frac{r}{R_{\text{min}}} \right)^{-2}, & R_{\text{min}} \leq r < R_{\text{in}} \\ \alpha \rho(R_{\text{min}}) \left(\frac{r}{R_{\text{min}}} \right)^{-2}, & R_{\text{in}} \leq r < R_{\text{out}} \\ \rho(R_{\text{min}}) \left(\frac{r}{R_{\text{min}}} \right)^{-2}, & R_{\text{out}} \leq r \leq R_{\text{max}}. \end{cases} \quad (1)$$

This model is similar to the treatment in Kerschbaum et al. (2010), where α was found to be 7000 (see their Table 2).

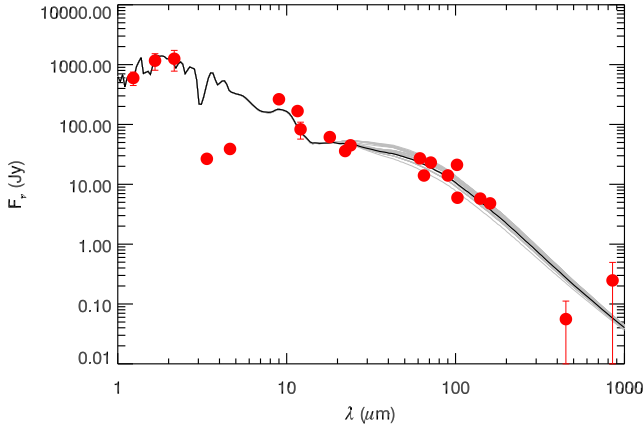
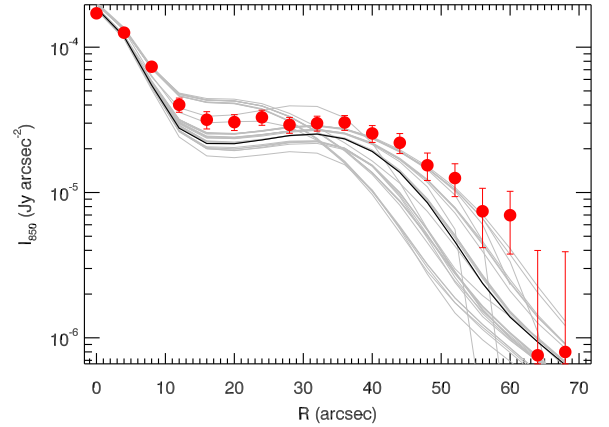
We now construct a grid of 2-DUST (Ueta & Meixner 2003) models exploring five parameters: $R_{\text{min}}, R_{\text{in}}, R_{\text{out}}, R_{\text{max}}$, and the enhancement α in the dust-production rate (DPR) in the detached shell. The inputs to the radiative transfer models are summarised in Table 1. We also list the optical depth in the shell, which is kept fixed at the value obtained from the GRAMS fit to the SED.

We perform radiative transfer for each combination of parameters in Table 1. Each model provides us with theoretical intensity profiles at each wavelength in the model spectrum. In order to compare these with the radial profile computed for U Ant in Section 3.2, we first compute synthetic photometry in the SCUBA2 filters, then convolve the resulting $850 \mu\text{m}$ intensity profile with the SCUBA2 PSF. We then find the best-fit parameters by minimising the reduced χ^2 comparing each model to the observed profile, and we also derive uncertainties for each parameter as the median absolute deviation from the median of each parameter. Table 2 shows the best-fit values and uncertainties for each parameter.

The best-fit DPR in the detached shell is $(8.2 \pm 0.2) \times 10^{-9} M_{\odot} \text{ yr}^{-1}$, and the total dust mass in the shell is $(0.98 \pm 0.15) \times 10^{-5} M_{\odot}$. Using a gas:dust ratio of 200, the corresponding gas mass-loss rate and gas mass are

Table 1. Input parameter grid for radiative transfer

R_{\min} (R_{star})	R_{in} ($''$)	R_{out} ($''$)	R_{out} ($''$)	α	τ_{ref} ($\times 10^{-3}$)
4.00, 5.00	26.0, 22.0, 34.0	56.0, 60.0, 44.0, 52.0, 48.0	60.0, 63.0, 66.0, 69.0, 72.0	750, 316	1.00

**Figure 4.** The best-fit model spectrum (thick line) to the SED of U Ant (red circles), including the SCUBA2 photometry. The range of models with acceptable fit quality (grey) are also shown.**Figure 5.** The best-fit model intensity profile at 850 μm (thick line) for the observed profile of U Ant (red circles). The range of models with acceptable fit quality (grey) are also shown.

$(1.64 \pm 0.04) \times 10^{-6} \text{ M}_{\odot} \text{ yr}^{-1}$ and $(1.96 \pm 0.30) \times 10^{-3} \text{ M}_{\odot}$ respectively.

The best-fit SED and intensity profile are shown in Figures 4 and 5. At 850 μm , all SED profiles including the best fit are on average a factor of four lower than the measured SCUBA-2 total flux. The derived intensity profiles at 850 μm , including the best fit intensity profile presented in Fig. 5 are also on average lower than the surface-brightness radial profile derived using the SCUBA-2 850 μm observation. This appears to be particularly significant in the inner region of the profile between $\sim 10'' - 30''$. Hence we see a similar sub-mm excess as previously reported by *Maercker et al., 2018, accepted, A&A*. The discrepancy in the amount of excess emission between *Maercker et al., 2018, accepted, A&A* and this study is partly due to the higher flux reported here, and partly due to the difference in modelling between the two studies.

4 DISCUSSION

4.1 Surface brightness emission

Fig. 1 show clear extended emission across the whole region of the detached shell reported in literature. The fraction of flux in the extended component (84%) is larger than any measured by *Dharmawardena et al. (2018)* in SCUBA-2 850 μm . We also see hints of an East-West asymmetry in the image plane. Similar hints appear to exist in the APEX/LABOCA data presented by *Maercker et al., 2018, accepted, A&A*. Deeper sub-mm data and/or improved processing techniques are required to confirm this asymmetry.

We see evidence for the detached shell in the surface brightness and residual profiles at 850 μm . The residual profile has a broad peak extending from 20'' to 40''. While the two inner optical scattered light sub-shells are located within this region, we do not see any evidence for distinct sub-shells therein. One reason for the lack of distinct sub-shells could be the resolution of our SCUBA-2 image; the separation between sub-shells is comparable to the FWHM of the SCUBA-2 beam (13''). Alternatively, this is evidence for the theory put forward by *Maercker et al. (2010)* where ss1 and ss2 are result of projected sub-structure in the two outermost sub-shells.

The extent at 3σ surface-brightness levels of 52'' coincides well with the outer edge of ss4 detected by *González Delgado et al. (2001, 2003)* and *Maercker et al. (2010)* in scattered light. This is also consistent with the outer-most shell reported by *Arimatsu et al. (2011)* in mid-IR. This radius lies within the interquartile range measured for the sample of fifteen sources by *Dharmawardena et al. (2018)* and would be the 5th-largest 3σ surface-brightness radius if it were included in the sample.

Assuming an outflow velocity of 20.5 km s^{-1} (*De Beck et al. 2010*) and a distance of 268 pc (*van Leeuwen 2007*), we trace the circumstellar shell out to an age of $3200 \pm 500 \text{ yr}$ at 850 μm at the 3σ level. This age is comparable to the ages obtained by *Maercker et al. (2010)*; *Kerschbaum et al. (2017)*.

The low SNR at 450 μm limits our ability to constrain the detached shell properties at this wavelength. However, the residual profile appear to have a possible peak at 40''. The additional effects of the large beam size of the

Table 2. Best-fit parameters and associated uncertainties resulting from the fit to the 850 μm intensity profile.

R_{min} (R_{star})	R_{in} ($''$)	R_{out} ($''$)	R_{out} ($''$)	α	τ_{ref} $\times 10^{-3}$	DPR $\times 10^{-9}$ ($\text{M}_{\odot} \text{ yr}^{-1}$)	M_{dust} $\times 10^{-6}$ (M_{\odot})	T_{in} (K)
5.0 ± 0	34 ± 0	52 ± 4.0	63 ± 3.0	320 ± 0	1.0 ± 0	8.2 ± 0.20	9.8 ± 1.5	1000 ± 0.016

observations does not allow us to constrain which dust shell is likely to emit in this region. Similar to 850 μm , due to the large beam size we cannot rule out contributions from other sub-shells, and it is not possible to determine which of the sub-shells is responsible for this emission.

The peaks at $\sim 41''$ and $\sim 39''$ in the 70 μm and 160 μm Herschel/PACS observations are consistent with the intensity peaks reported by Kerschbaum et al. (2010) and Cox et al. (2012) using the same data. They conclude the detached shell to be a single shell at $\sim 42''$, most likely corresponds to ss3. They are also consistent with the single gas-rich shell reported by Kerschbaum et al. (2010) using ALMA observations. Hence it is possible that ss3 also emits in the dust continuum. Kerschbaum et al. (2017) suggests this gas-rich shell to have strong gas and dust coupling resulting in the peaks observed in both the CO observations and dust continuum observations. However the exact mechanism causing ss3 to contain both gas and dust, while causing the other sub-shells to be gas poor, is puzzling and not yet well understood.

Comparison of SCUBA-2 data with Herschel/PACS observations reveal further peculiarities of the detached shell. The emission enhancement observed in the inner region of the SCUBA-2 850 μm residual profile implies that SCUBA-2 850 μm detects emission from the total detached shell but is dominated by emission from the inner region. However the peaks observed in the PACS residual profiles imply that they are dominated by the outermost regions of the detached shell. A simple interpretation of this is that the 850 μm observations are sensitive to an additional component in the inner region that is too cold for Herschel to detect. However this is unlikely as the dust temperatures required for such a component is expected to be ~ 4 K from Wien's law, which is not seen in Fig. 3. Normally we expect the dust closer to the central star to be warmer, contrary to what we observe. In order for warmer dust to contribute more to the emission at 850 μm than at 160 μm it must have significantly different dust properties. The sub-mm excess of U Ant detailed in Sec. 3.3 could be related to this phenomenon. In this case, larger or more amorphous grains may be preferentially located in the inner ejecta, enhancing the sub-mm emission from this region.

4.2 Radial variation in dust properties

In Figure 3 we present the T , Σ and β SED fitting results calculated using MCMC model fitting. Due to PSF subtraction effects we ignore the innermost $\sim 10''$ region of all three profiles.

We observe a clear decreasing gradient in the inner $\sim 30''$ of the T profile consistent with that of an optically-thin centrally-heated spherical dust shell. Following this region there is a transition in the T profile, which becomes

more-or-less flat (up to ~ 55 from where the priors dominate) as expected with dust heated by a uniform Interstellar radiation field (ISRF). The overall shape and features observed for the T profile U Ant is consistent with that of the sample of evolved stars presented in Dharmawardena et al. (2018), with clear analogues to the detached shell source in the sample, U Hya.

We measure a weighted average temperature of 51 ± 1 K for this flat region agreeing well with the dust temperature of 55 ± 20 K determined by Schöier et al. (2005) using radiative transfer modelling. Dust grains in this regions are heated by the same uniform ISRF and hence possess the same temperature distribution, giving rise to a single-temperature dust component.

As expected for a detached shell source, akin to the detached shell source U Hya analysed in Dharmawardena et al. (2018), it is clear from the middle panel in Fig. 3 the radial variation in Σ deviates from the uniform and constant mass-loss model overlaid in orange. The broad Σ enhancement corresponds with the total detached shell region and we do not see evidence for multiple shells within it.

We observe a sudden decrease in the Σ profile at $52''$, coinciding with the outer edge of detached shell at 850 μm . This is also consistent with the outer edge determined from optical observations. Considering look-back time we interpret this to be a sudden increase in mass-loss about 3200 ± 500 yr ago. Therefore we expect the thermal pulse which gave rise to the detached shell to have occurred approximately 3200 ± 500 yr in the past, concurring with previous results (Maercker et al. 2010; Kerschbaum et al. 2017).

The integrated dust mass derived from this density enhancement is $2.2 \times 10^{-4} \text{ M}_{\odot}$. Using the simple approximation of evenly distributed dust we derive a sub-shell mass of $\sim 5.5 \times 10^{-5} \text{ M}_{\odot}$ per sub-shell, which is then consistent with the dust mass of sub-shell four determined by Maercker et al. (2010). However grain property and sub-shell dust-to-gas ratio variations observed means a more in-depth calculation is required in order to accurately compare sub-shell masses.

Kerschbaum et al. (2010) derive a total detached shell dust mass of $1.6 \times 10^{-7} \text{ M}_{\odot}$ (assuming a gas:dust ratio of 200) using radiative-transfer modelling. Arimatsu et al. (2011) also follow radiative-transfer modelling methods to derive a dust mass of $1.6 \times 10^{-5} \text{ M}_{\odot}$, but only for sub-shells three and four. Both these dust masses are at least a magnitude less than the total dust mass we derive. Similarly the dust mass derived via radiative-transfer modelling in this study is a factor of twenty-two less than the dust mass derived from the Σ profile. We can attribute this difference to two causes. Firstly, we are sensitive to dust in the total detached shell rather than being limited to a few sub-shells. Secondly, we are including sub-mm wavelengths in the mass determination and converting flux into mass. A higher flux at longer wavelengths therefore implies higher

masses. As noted at the end of Sec. 3.3 above, we measure an excess emission at $850\ \mu\text{m}$ and we see more $850\ \mu\text{m}$ emission than might be expected given the Herschel observations.

Conversely though also using radiative transfer modelling the total dust mass of the detached derived by Schöier et al. (2005), $(1.3 \pm 1.2) \times 10^{-4}\ M_{\odot}$, is well matched with the dust mass derived by us. Therefore we must note that the total detached shell dust mass varies over a wide range in multiple wavelengths, studies and methods.

The final panel in Fig. 3 depicts the radial β variation of the detached shell. The negative gradient seen from $\sim 10''$ to $\sim 30''$ corresponds with the decreasing region of the T profile. This indicates a significant difference in the properties of dust (e.g. size, shape or composition) in this inner region compared to the outer region of the shell. This may also be related to the origin of the sub-mm excess; if grains with a lower β are preferentially in this inner region of the shell, it will tend to produce more sub-mm emission. This could occur if larger grains are present or if the abundance of amorphous (rather than graphitic) grains is higher in this region of the shell.

Following this inner region we see an increasing trend with some slight variations. Here it is likely we are observing grain property variations with a minimum β of 1.65 and a maximum of 1.85. These β results can be interpreted as being intermediate to the expected values for amorphous carbon and graphite (Mennella et al. 1998; Draine 2016). Finally the region beyond $R_{3\sigma}$ (i.e: $52''$), is dominated by the prior as its best-fit value is dictated by the SCUBA-2 data, which no longer provide strong constraints.

4.3 Self-consistent dust radiative transfer modelling

The outer radius of the shell coincides with the extent at 3σ surface-brightness level in the SCUBA-2 data. The inner radius, on the other hand, coincides with the inner edge of ss2 derived by González Delgado et al. (2001). However, the value of α differs from that derived by Kerschbaum et al. (2017) by a factor of ~ 20 ; this is a result of the larger width of the shell in our model compared to the gas shell modelled by Kerschbaum et al. (2017).

The total dust mass falls within the range reported by similar radiative-transfer studies in the past, taking into account the uncertainties that arise from different ways of computing the dust opacities. Kerschbaum et al. (2010) used a Continuous Distribution of Ellipsoids to compute cross-sections, which can produce a higher sub-mm opacity and hence a smaller dust mass, which is likely to be a significant contributor to the 10^2 difference in dust masses. In addition, they used amorphous carbon refractive indices from Preibisch et al. (1993), which give consistently higher sub-mm opacities than those from Zubko et al. (1996) used in GRAMS. On the other hand, our result is within a factor of a few of the results of Arimatsu et al. (2011), which seems reasonable given the difference in how the model was specified. However, the mass derived from radiative-transfer modelling is an order of magnitude lower than that derived by fitting modified blackbodies to each point in the radial profiles. As mentioned above, this is probably a result of the fact that the modified blackbody fitting will simply increase the mass

to explain the observed flux, and hence the presence of the sub-mm excess will result in a higher dust mass in that case.

However, the best-fitting models systematically underestimate the flux outside the central point source of the SCUBA-2 $850\ \mu\text{m}$ radial profile. The geometry of U Ant is known to be more complex than we have assumed, and this may indicate that more free parameters are required to successfully describe the shell. Should this be related to observed sub-mm excess it would imply that the entire shell contributes to the excess emission, but it is dominated by the inner region of the detached shell.

5 CONCLUSIONS

We present a resolved detection of the detached shell of U Ant in submillimetre continuum using JCMT/SCUBA-2 observations. The detached shell is clearly detected at $850\ \mu\text{m}$ and marginally at $450\ \mu\text{m}$. The detached shell's 3σ extent at $850\ \mu\text{m}$ is traced out to $52''$ ($0.07 \pm 0.01\ \text{pc}$), consistent with past publications. The residual profile has a broad peak between $20''$ to $40''$. However, similar to CO emission and unlike optical scattered light observations, we do not see the detached shell in the sub-mm separate into multiple sub-shells. Therefore it is likely these optical scattered light sub-shells are indeed a result of projected sub-structure of the outer sub-shells. However we may also not be seeing these multiple sub-shells in the sub-mm due resolution and large beam size effects. Higher sensitivity SCUBA-2 observations combined with high-resolution interferometric observations such as with ALMA of the sub-mm dust continuum will allow us to test this scenario.

Radiative-transfer model fitting of the shell predicts a geometrically-thick dust shell stretching from $\sim 34 - 52''$, broadly consistent with the literature and with the SCUBA-2 radial profile. However, it underestimates the contribution of the shell to the total flux. This underestimate is largest in the inner region between $10'' - 30''$. Hence implying the presence of a sub-mm excess at $850\ \mu\text{m}$ when compared to model predictions.

Curiously while the location of the peaks in the Herschel/PACS residual profiles imply that the far-IR observations are dominated by the outer region of the detached shell, the broad peak seen in the residual profile at $850\ \mu\text{m}$ implies that the sub-mm observations are dominated by a dust component with significantly different properties in the inner region of the detached shell. This could be the cause for the sub-mm excess observed in U Ant. Hence if the largest dust grains are preferentially in the inner region, this could lead to stronger sub-mm emission in the inner regions of the detached shell. This then implies there may indeed have been gas-grain decoupling as a result of a reverse shock front in the detached shell causing multiple velocity separated dust components with varying grain properties. While this scenario was put forward as the cause for the inner sub-shells the reverse shock front and the resulting decoupled dust may not necessarily lead to sub-shell per say. It could also result in clumps or filaments (as suggested by Kerschbaum et al. (2017)) in the inner region visible as single continuous emission bump in the sub-mm.

The sudden mass-loss increase in the Σ profile at $52''$ points to the time of the thermal pulse which gave rise to

the detached shell. We calculate it to have occurred approximately 3200 ± 500 yr in the past, coinciding with past results. By integrating over the Σ enhancement observed we estimate a total shell dust mass of $2.2 \times 10^{-4} M_{\odot}$. This dust mass is approximately a magnitude greater than several dust masses determined via radiative transfer modelling. It is likely this is the product of the aforementioned sub-mm excess. The β profile indicate the presence of amorphous Carbon in the detached shell. However again the sub-mm excess may have affected these β values and as a result they maybe greater than expected.

ACKNOWLEDGEMENTS

Thavisha Dharmawardena wishes to thank Prof. Chung-Ming Ko at NCU for his support of this project. We are grateful to Mattias Maeker for the engaging discussions on the topic. This research has been supported under grant MOST104-2628-M-001-004-MY3 from the Ministry of Science and Technology of Taiwan. IM acknowledges support from the UK Science and Technology Facility Council under grant ST/P000649/1.

The James Clerk Maxwell Telescope is operated by the East Asian Observatory on behalf of The National Astronomical Observatory of Japan; Academia Sinica Institute of Astronomy and Astrophysics; the Korea Astronomy and Space Science Institute; the Operation, Maintenance and Upgrading Fund for Astronomical Telescopes and Facility Instruments, budgeted from the Ministry of Finance (MOF) of China and administrated by the Chinese Academy of Sciences (CAS), as well as the National Key R&D Program of China (No. 2017YFA0402700). Additional funding support is provided by the Science and Technology Facilities Council of the United Kingdom and participating universities in the United Kingdom and Canada. *Herschel* is an ESA space observatory with science instruments provided by European-led Principal Investigator consortia and with important participation from NASA. In addition to software cited above, this research made use of the *Scipy* (Jones et al. 2001) and *Astropy* (The Astropy Collaboration et al. 2018) python packages. This research used the facilities of the Canadian Astronomy Data Centre operated by the National Research Council of Canada with the support of the Canadian Space Agency. This research also made use of the Canadian Advanced Network for Astronomical Research (CANFAR) (Gaudet et al. 2010).

REFERENCES

- Arimatsu K., Izumiura H., Ueta T., Yamamura I., Onaka T., 2011, *ApJ*, **729**, L19
- Beichman C. A., Neugebauer G., Habing H. J., Clegg P. E., Chester T. J., eds, 1988, *Infrared astronomical satellite (IRAS) catalogs and atlases. Volume 1: Explanatory supplement Vol. 1*
- Bowen G. H., Willson L. A., 1991, *ApJ*, **375**, L53
- Boyer M. L., et al., 2012, *ApJ*, **748**, 40
- Cox N. L. J., et al., 2012, *A&A*, **537**, A35
- Currie M. J., Berry D. S., Jenness T., Gibb A. G., Bell G. S., Draper P. W., 2014, in Manset N., Forshay P., eds, *Astronomical Society of the Pacific Conference Series Vol. 485, Astronomical Data Analysis Software and Systems XXIII*. p. 391
- De Beck E., Decin L., de Koter A., Justtanont K., Verhoelst T., Kemper F., Menten K. M., 2010, *A&A*, **523**, A18
- Dharmawardena T. E., et al., 2018, *Monthly Notices of the Royal Astronomical Society*, **479**, 536
- Doi Y., et al., 2015, *PASJ*, **67**, 50
- Doty S. D., Leung C. M., 1994, *ApJ*, **424**, 729
- Draine B. T., 2016, *ApJ*, **831**, 109
- Foreman-Mackey D., Hogg D. W., Lang D., Goodman J., 2013, *PASP*, **125**, 306
- Gaudet S., et al., 2010, in *Software and Cyberinfrastructure for Astronomy*. p. 77401I, doi:10.1117/12.858026
- González Delgado D., Olofsson H., Schwarz H. E., Eriksson K., Gustafsson B., 2001, *A&A*, **372**, 885
- González Delgado D., Olofsson H., Schwarz H. E., Eriksson K., Gustafsson B., Gledhill T., 2003, *A&A*, **399**, 1021
- Gordon K. D., et al., 2014, *ApJ*, **797**, 85
- Groenewegen M. A. T., et al., 2011, *A&A*, **526**, A162
- Hildebrand R. H., 1983, *QJRAS*, **24**, 267
- Höfner S., 2008, *A&A*, **491**, L1
- Höfner S., Olofsson H., 2018, *A&ARv*, **26**, 1
- Holland W. S., et al., 2013, *MNRAS*, **430**, 2513
- Ishihara D., et al., 2010, *A&A*, **514**, A1
- Izumiura H., Hashimoto O., Kawara K., Yamamura I., Waters L. B. F. M., 1996, *A&A*, **315**, L221
- Izumiura H., Waters L. B. F. M., de Jong T., Loup C., Bontekoe T. R., Kester D. J. M., 1997, *A&A*, **323**, 449
- Izumiura H., et al., 2011, *A&A*, **528**, A29
- Jenness T., Stevens J. A., Archibald E. N., Economou F., Jessop N. E., Robson E. I., 2002, *MNRAS*, **336**, 14
- Jones E., Oliphant T., Peterson P., et al., 2001, *SciPy: Open source scientific tools for Python*, <http://www.scipy.org/>
- Karakas A. I., Lattanzio J. C., 2014, *Publ. Astron. Soc. Australia*, **31**, e030
- Kerschbaum F., et al., 2010, *Astronomy and Astrophysics*
- Kerschbaum F., et al., 2017, *A&A*, **605**, A116
- Maercker M., Olofsson H., Eriksson K., Gustafsson B., Schöier F. L., 2010, *A&A*, **511**, A37
- Maercker M., et al., 2012, *Nature*, **490**, 232
- Maercker M., Silva T. K., Beck E. D., Brunner M., Mecina M., Jaldehag O., 2018, *A&A*
- Marigo P., et al., 2017, *ApJ*, **835**, 77
- Mennella V., Brucato J. R., Colangeli L., Palumbo P., Rotundi A., Bussolletti E., 1998, *ApJ*, **496**, 1058
- Neugebauer G., et al., 1984, *ApJ*, **278**, L1
- Olofsson H., Eriksson K., Gustafsson B., 1988, *A&A*, **196**, L1
- Olofsson H., Carlstrom U., Eriksson K., Gustafsson B., Willson L. A., 1990, *A&A*, **230**, L13
- Olofsson H., Maercker M., Eriksson K., Gustafsson B., Schöier F., 2010, *A&A*, **515**, A27
- Preibisch T., Ossenkopf V., Yorke H. W., Henning T., 1993, *A&A*, **279**, 577
- Ramstedt S., Maercker M., Olofsson G., Olofsson H., Schöier F. L., 2011, *A&A*, **531**, A148
- Sadavoy S. I., et al., 2013, *ApJ*, **767**, 126
- Sargent B. A., Srinivasan S., Meixner M., 2011, *ApJ*, **728**, 93
- Schöier F. L., Lindqvist M., Olofsson H., 2005, *A&A*, **436**, 633
- Shetty R., Kauffmann J., Schnee S., Goodman A. A., Ercolano B., 2009, *ApJ*, **696**, 2234
- Simis Y. J. W., Icke V., Dominik C., 2001, *A&A*, **371**, 205
- Skrutskie M. F., et al., 2006, *AJ*, **131**, 1163
- Srinivasan S., Sargent B. A., Meixner M., 2011, *A&A*, **532**, A54
- The Astropy Collaboration et al., 2018, preprint, ([arXiv:1801.02634](https://arxiv.org/abs/1801.02634))
- Ueta T., Meixner M., 2003, *ApJ*, **586**, 1338
- Vassiliadis E., Wood P. R., 1994, *ApJS*, **92**, 125
- Villaver E., García-Segura G., Manchado A., 2002, *ApJ*, **571**, 880
- Willems F. J., 1988, *A&A*, **196**, 173
- Wright E. L., et al., 2010, *AJ*, **140**, 1868

- Zijlstra A. A., Chapman J. M., te Lintel Hekkert P., Likkel L.,
Comeron F., Norris R. P., Molster F. J., Cohen R. J., 2001, [MNRAS](#), **322**, 280
- Zubko V. G., Mennella V., Colangeli L., Bussoletti E., 1996, [MNRAS](#), **282**, 1321
- van Leeuwen F., 2007, [A&A](#), **474**, 653

APPENDIX A: SCHEMATIC DIAGRAM OF U ANT

APPENDIX B: SCUBA OBSERVATIONS

The 1997 SCUBA image regrettably was noise dominated and could not be included in our analysis. However the reduced image (see Fig. B1) show a roughly circular pattern of blobs at $\sim 24''$ and $\sim 48''$ from the position of the central star. The outer circular pattern is at a similar radius to that of the SCUBA-2 850 μm 3σ surface brightness extent derived below.

U Ant was observed for project M96BI17 on 19971017 and 19971020 for a total of 2.1 hours. The data were re-processed using the SURF package and with the standard calibration factor for the 850N filter at the largest available aperture size of 60 arcsec [Jenness et al. \(2002\)](#). The reduction process included correction for opacity using skydips taken around the observations (yielding $\tau(850, \text{zenith})$ of 0.28-0.41); cleaning with a 5-sigma clip, despiking, sky removal and bolometer weighting; and map reconstruction with median-regridding in 3 arcsec pixels, matching the native sampling of jiggle observations. The map was then smoothed with a 9 arcsec gaussian to an effective resolution of approximately 17 arcsec FWHM. There is no information in the map on scales larger than the 2 arcmin chop throw, so the true zero level is poorly established. The radial profile is around an estimated overall flux-centroid of 10:35:13.0, -39:33:52 (J2000), south of the expected stellar position (attributed to a poor pointing model at far-south Declinations). The noise is estimated from the dispersion among pixels in each annulus, converted to a standard error based on the number of independent beams within the annulus.

APPENDIX C: TABLE OF FLUXES USED IN RT MODELLING

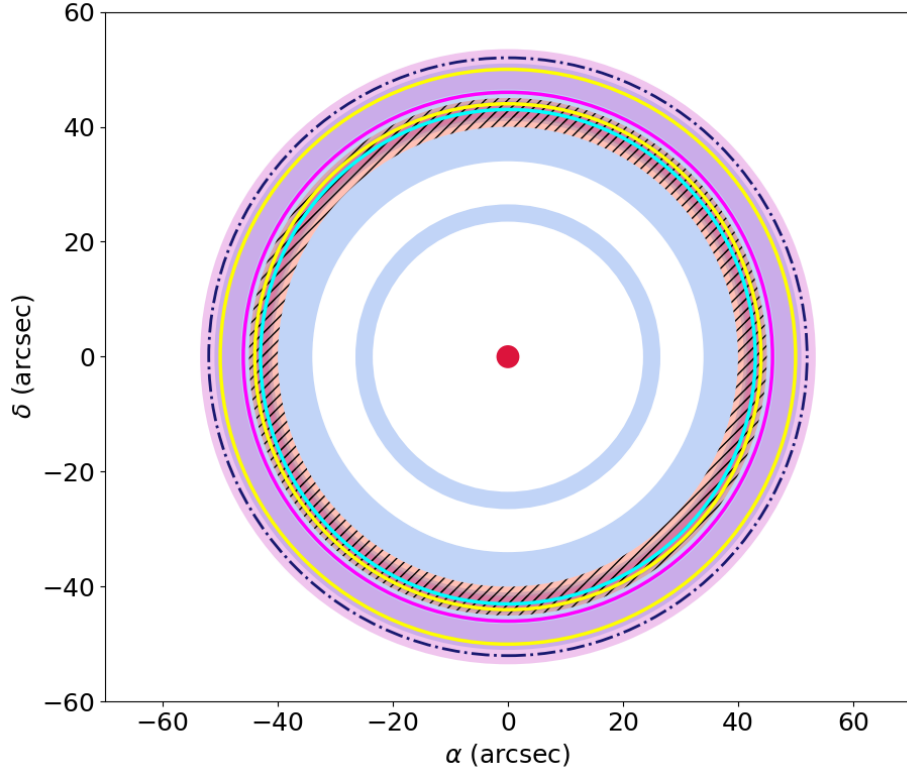


Figure A1. Schematic Diagram of U Ant. The dots represent sub-shells determined to be dust-rich and the hashed lines represents the sub-shells determined to be gas-rich. The colours separate out the various publications the sub-shell radii and widths are drawn from. The annuli represent sub-shell with the widths given in their respective publications. Sub-shells with only mean radii and no widths are presented in the form of a solid line. The dot-dashed outermost radius shows the 3σ surface brightness extent determined in this work. The colours used and sub-shell details are presented in Tab. A1

Table A1. Published Shell Parameters of U Ant

Publication	Mean Shell Radius (")	Shell Thickness (")	Colour of sub-shell in Fig. A1
Izumiura et al. (1997)	46	–	Magenta
	180	Not included here	solid line
González Delgado et al. (2001)	25	3	Light blue
and	37	6	filled annulus
González Delgado et al. (2003)	43	3	
	46	10	
Maercker et al. (2010)	43	2	Light pink
	50	7	filled annulus
	43	2.6	
Arimatsu et al. (2011)	44	–	Yellow
	50	–	solid line
Cox et al. (2012)	42	–	Cyan
			solid line
Kerschbaum et al. (2017)	42.5	5	Light red
			filled annulus
3σ surface brightness extent derived in this paper	52	–	Dark blue dot-dashed line

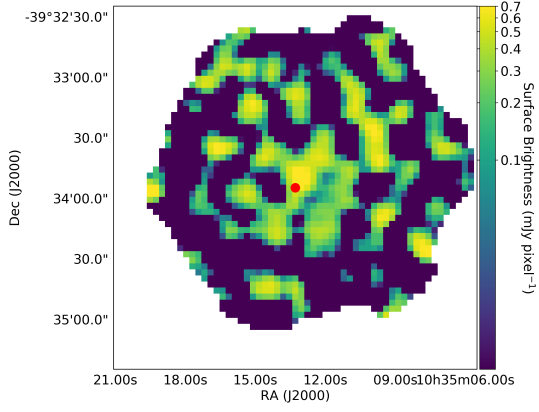


Figure B1. SCUBA 850 μm observation of U Ant from 1997. The off-centred red dot indicates the position of the star. It is off centre due to pointing accuracy problems in SCUBA.